

Near- and far-infrared p -GaAs dual-band detector

G. Ariyawansa, M. B. M. Rinzan, D. G. Esaev, S. G. Matsik,
G. Hastings, and A. G. U. Perera^{a)}

Department of Physics and Astronomy, Georgia State University, Atlanta, Georgia 30303

H. C. Liu

Institute for Microstructural Sciences, National Research Council, Ottawa KIA OR6, Canada

B. N. Zvonkov and V. I. Gavrilenko

Institute for Physics of Microstructures, Nizhny Novgorod, Russia

(Received 2 December 2004; accepted 22 February 2005; published online 1 April 2005)

A dual-band homojunction interfacial workfunction internal photoemission infrared detector that responds in both near- and far-infrared (NIR and FIR) regions is reported. In the p^+-i-p^+ detector structure, the emitter is carbon doped to $1.5 \times 10^{19} \text{ cm}^{-3}$, and a $1 \mu\text{m}$ thick GaAs layer acts as the barrier, followed by another highly p -doped GaAs contact layer. The NIR response is due to the interband transition in GaAs barrier layer and the threshold wavelength observed at $0.82 \mu\text{m}$ is in good agreement with the 1.51 eV band gap of GaAs at 4.2 K. The intraband transition giving rise to FIR response is observed up to $70 \mu\text{m}$. Interband responsivity was (under 100 mV reverse bias at 20 K) $\sim 8 \text{ A/W}$ at $0.8 \mu\text{m}$, while the intraband responsivity was $\sim 7 \text{ A/W}$. The detector has peak detectivities $D^* \sim 6 \times 10^9$ and $5 \times 10^9 \text{ cm Hz}^{1/2}/\text{W}$ at 0.8 and $57 \mu\text{m}$ wavelengths, respectively, under 100 mV reverse bias at 20 K. © 2005 American Institute of Physics. [DOI: 10.1063/1.1899242]

In addition to the astronomy applications, multiband detectors would be useful in numerous other applications. While recently reported dual-band^{1,2} and multiband³⁻⁵ detectors can detect near-infrared (NIR) and mid-infrared (MIR) radiation, the reported detector has the ability to detect NIR, MIR, and far-infrared (FIR) radiation up to $70 \mu\text{m}$. In applications such as mine detection,¹ the use of images in two different spectral bands can aid in the detection and can reduce the number of false positives. The NIR portion of the detector could also be used to detect the muzzle flash to locate the position of enemy troops, while the FIR radiation is useful for determining troops and operating vehicles. Moreover, a multiband detector can be used as a remote thermometer by taking the difference in the spectral information of the signal for the two bands.

The reported homojunction interfacial workfunction internal photoemission (HIWIP) detector consists of a $1.5 \times 10^{19} \text{ cm}^{-3}$ carbon-doped emitter layer and a barrier layer that is placed in between two conducting layers used as the top contact and the bottom contact. The Fermi level in the emitter layer lies above the valence band edge of the barrier layer, producing an interfacial workfunction that determines the FIR threshold wavelength. So far, reported HIWIP FIR detectors^{6,7} have been focused mainly on the intraband transitions within the structure. In this letter, a GaAs-based HIWIP detector is presented that can be operated in NIR and MIR/FIR regions due to interband and intraband transitions in the detector structure, respectively. By replacing the As with N, that is, by using GaN material system, the ability to extend the NIR response up to UV will also be discussed.

The HIWIP sample was grown by the metalorganic chemical vapor deposition technique at $610 \text{ }^\circ\text{C}$ on a semi-insulating GaAs (100) substrate. The structure consists of a

bottom contact (p^{++}) layer with $1.0 \mu\text{m}$ thickness, a barrier layer with $1.0 \mu\text{m}$ thickness, an emitter (p^+) layer with $0.2 \mu\text{m}$ thickness, and a top contact layer. However, the top contact and a part of the emitter layer were etched out, leaving about an 800 \AA thick emitter region (out of $0.2 \mu\text{m}$) as shown in Fig. 1(a), in order to process mesas for characterization. The layer parameters (thickness and doping level) of the sample was confirmed by secondary-ion mass spectrometry (SIMS). The mesas have different sizes of optical windows, and the spectral measurements were carried out on a mesa with a $460 \mu\text{m} \times 460 \mu\text{m}$ optical window.

The band diagram of the structure is shown in Fig. 1(b). The photons with energy above the band gap (NIR) are absorbed in the barrier, giving rise to a transition of carriers (electron-hole pair) between the conduction and valence band of the GaAs barrier. The electron-hole pairs generated in the emitter would have to undergo internal photoemission before being collected. This process is same as MIR-generated carriers (intraband transition) in the emitter. Incident photons with energy below the band gap (MIR/FIR), absorbed in the emitter layer (free carrier absorption) photoexcite carriers, which then undergo internal photoemission across the barrier. The offset between the Fermi level in p -doped emitter layer and the valence band of GaAs barrier is defined as the interfacial workfunction (Δ), which determines the FIR threshold wavelength. The photoexcited carriers are finally swept out of the active region and are collected at the contact by the applied electric field. The detector was characterized by current-voltage (I - V) and spectral responsivity measurements from 4.6 to 20 K. The spectra were obtained using a System 2000 Perkin Elmer Fourier transform infrared spectrometer with three beam splitters. The calibration of spectra was done by using a spectrum obtained with a Si composite bolometer with the same combination of optical components. Since the detector responds

^{a)}Electronic mail: uperera@gsu.edu

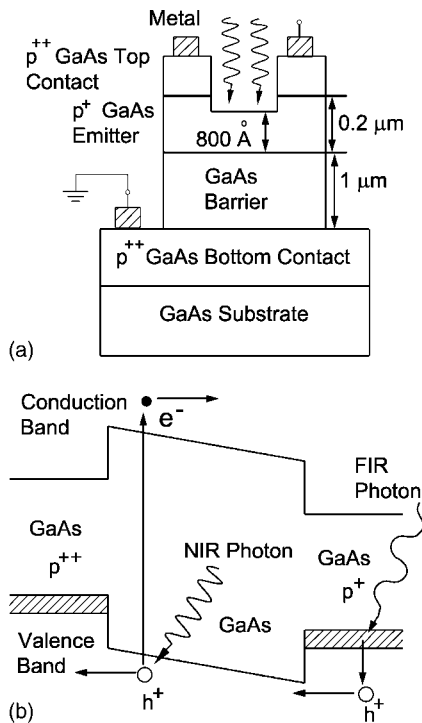


FIG. 1. (a) Schematic of *p*-GaAs single-emitter HIWIP dual-band detector after processing. The top contact, emitter, barrier, and bottom contact have thicknesses of 120 nm, 200 nm, 1.0 μm , and 1 μm , respectively. A window on the top of the device is made for front side illumination, leaving only about 800 \AA as the emitter thickness. (b) The band diagram for HIWIP dual-band detector indicating both interband and intraband transitions leading to NIR and MIR/FIR responses.

in both bands under the same conditions, it is not tunable without exterior optical filtering.

The NIR spectral response due to interband transition of carriers in GaAs barrier layer is shown in Fig. 2. The solid line represents the experimental curve for 100 mV reverse bias, while the dashed line represents the calculated curve based on a model⁷ in which the absorption coefficient for interband was calculated using the permittivity model in Ref. 8. With the band gap in GaAs being 1.51 eV, the threshold wavelength observed at 0.82 μm confirms the interband transition in GaAs. The optimum responsivity at 0.8 μm is ~ 9 A/W, while the detectivity is $\sim 2.7 \times 10^{11}$ $\text{cm Hz}^{1/2}/\text{W}$ under 100 mV reverse bias at 4.6 K. The oscillations seen in

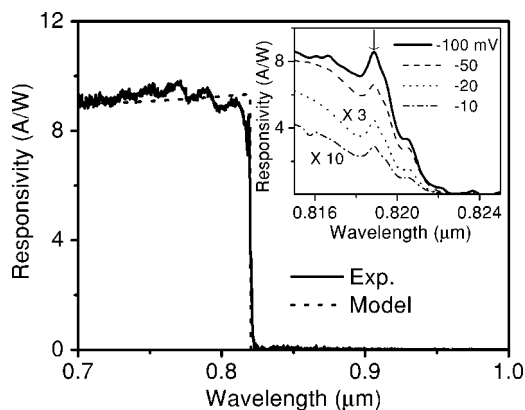


FIG. 2. The interband response fitted with a model for 100 mV reverse bias. The inset shows the bias dependence of the exciton peak at the threshold end of the experimental response curve. The two curves for 10 and 20 mV reverse bias have been multiplied by 10 and 3, respectively, for clarity.

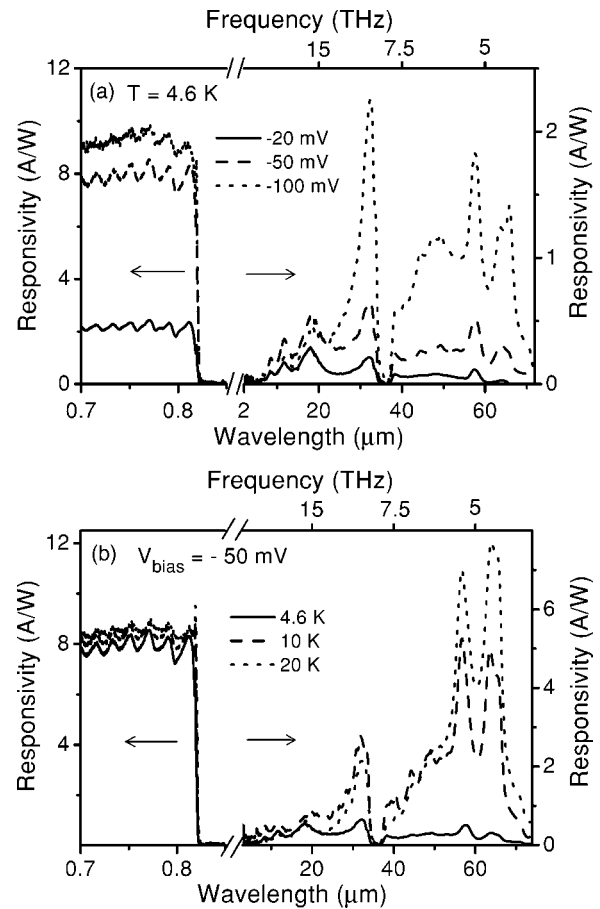


FIG. 3. (a) Interband and intraband responses at 4.6 K under different reverse bias values. (b) Interband and intraband response at different temperatures under -50 mV bias. The left and right axes are the NIR and FIR responsivities, respectively, and a break on the wavelength axis at 2 μm has been made in order to expand the view in both regions.

the NIR region diminishes with the applied electric field and the temperature. As shown in the inset to Fig. 2, the small peak at 0.819 μm (1.514 eV) is due to excitons⁹ in GaAs and the amplitude of this peak increases with increasing bias.

The spectral response for different bias voltages in both NIR and FIR regions at 4.6 K is given in Fig. 3(a). The response due to intraband transition is observed up to 70 μm and it has a responsivity of ~ 1.8 A/W and a detectivity of $\sim 5.6 \times 10^{10}$ $\text{cm Hz}^{1/2}/\text{W}$ at 57 μm under 100 mV reverse bias. Since the interband response is optimum at 100 mV reverse bias, Fig. 3(a) shows the spectra for both bands only up to 100 mV reverse bias. The oscillations in the MIR region observed are due to Fabry-Perot interference arising from the 1 μm thick GaAs barrier layer in the device structure. The sharp drop around 37 μm is due to the strong absorption around the reststrahlen band of GaAs. The two peaks at 57 and 63 μm are due to transitions of hydrogenic-like impurity atoms in the barrier region from the impurity ground state to the excited states.⁷ These transitions show a strong bias dependence due to the fact that the carriers excited to upper states undergo tunneling through the barrier, formed by the Coulomb potential of acceptors, with the support of the external applied field.

The spectral responsivity curves due to both interband and intraband transitions measured from 4.6 to 20 K are shown in Fig. 3(b). An optimum responsivity of ~ 8 A/W and a detectivity of $\sim 6 \times 10^9$ $\text{cm Hz}^{1/2}/\text{W}$ were obtained at

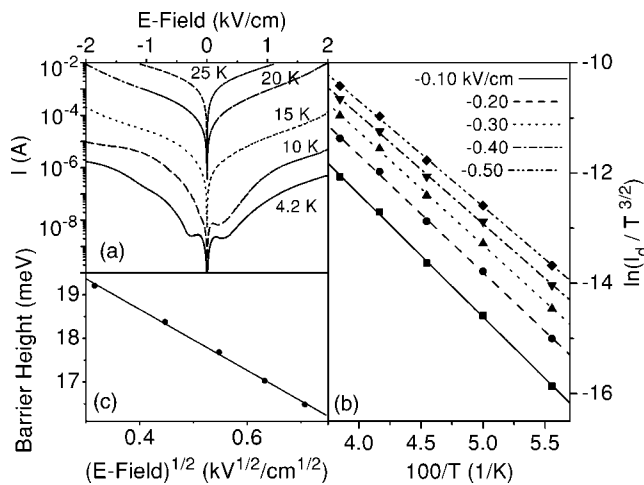


FIG. 4. (a) IV curves at different temperatures under dark condition. The asymmetry in the IV is probably due to the asymmetry in the structure. (b) The Arrhenius curves under different reverse electric fields, while (c) shows the variation of calculated effective barrier height based on Arrhenius plot with the square root of applied electric field.

$0.8 \mu\text{m}$ for interband response, while a responsivity of $\sim 7 \text{ A/W}$ and a detectivity of $\sim 5 \times 10^9 \text{ cm Hz}^{1/2}/\text{W}$ were reported at $57 \mu\text{m}$, under 100 mV reverse bias at 20 K . The responsivity of 63 and $57 \mu\text{m}$ peaks show strong dependence with the temperature and the $63 \mu\text{m}$ peak is relatively high at higher temperatures. This is caused, presumably, by the increased rate of collecting carriers excited to the upper states from the impurity ground state. If the rate of collection of excited carriers by the external circuit is low, the excited carriers either will relax back in to the ground state or can occupy the excited states, resulting in a high population density. At high temperature, the rate of collection of excited carriers over the barrier can be enhanced by the thermal energy, leading to enhanced responsivity.

The variation of the dark current at different temperatures are given in Fig. 4(a). The asymmetry in the IV curve is due to the asymmetry in the structure. Arrhenius plots under different reverse electric fields are shown in Fig. 4(b); the dots represent the experimental data while lines represent the linear fit. The effective barrier height (Δ) can be calculated from the slope of the fitted lines. The Fig. 4(c) shows the dependence of effective barrier height on square root of applied field and the fitted line denotes that the effective barrier height has a linear relationship with the square root of the applied electric field. Δ increases with the applied bias⁶ giving rise to an increasing threshold with bias. At a 0.20 kV/cm field, Δ is 18.4 meV corresponding to a $67.5 \mu\text{m}$ threshold, and similarly at a 0.50 kV/cm field, the Δ is 16.5 meV , giving a $75 \mu\text{m}$ threshold. These results are consistent with the spectral response curves shown in Fig. 3(a).

In order to detect UV along with IR, a modification of the HIWIP structure with GaN/AlGaIn is also feasible. Using an n^+-i-n^+ structure, a GaN/AlGaIn/GaN UV detector

can detect UV radiation by interband absorption in the AlGaIn layer. UV detectors have already been demonstrated by several groups^{10,11} using GaN/AlGaIn system. Intraband transitions giving rise to IR absorption in GaN/AlGaIn will be similar to that in GaAs/AlGaAs heterojunction interfacial workfunction internal photoemission detectors.¹² The IR photons will be absorbed in the heavily doped GaN emitter layer, photoexciting the electrons within the conduction band. Due to strong TO phonon-photon interaction and phonon absorption, a deep valley at $\sim 18 \mu\text{m}$ in the responsivity curve of a GaN/AlGaIn detector ($\sim 37 \mu\text{m}$ for GaAs/AlGaAs) is expected. Compared to the GaAs/AlGaAs system, GaN/AlGaIn has advantages in controlling the Al fraction over a wide range and the broad continuous spectral response range. Even though GaN/AlGaIn detectors are expected to behave similarly to HIWIP dual-band detector reported in this letter, such a detector has yet to be demonstrated experimentally.

In summary, a HIWIP detector that can detect NIR and MIR/FIR radiation is reported. Based on a theoretical model and experimental data, the transition in the GaAs based structure giving rise to NIR and MIR/FIR response is explained. High performance of the detector demonstrates the potential applications wherein the detection in both NIR and MIR/FIR is important. Using a different material system such as GaN/AlGaIn instead of GaAs/AlGaAs can extend the detection capability of the detector into the UV range, providing a dual-band detector covering UV and FIR regions.

This work is supported in part by the NSF under Grant Nos. ECS-0140434 and DBI: 0352324. The authors thank R. Dudek, T. Oogarah, and K. Liu for sample preparation and S. Rolfe for SIMS measurement.

¹A. Goldberg, P. N. Uppal, and M. Winn, *Infrared Phys. Technol.* **44**, 427 (2003).

²H. C. Liu, P. H. Wilson, M. Lamm, A. G. Steele, Z. R. Wasilewski, Jianming Li, M. Buchanan, and J. G. Simmons, *Appl. Phys. Lett.* **64**, 475 (1994).

³S. Raghavan, P. Rotella, A. Stintz, B. Fuchs, S. Krishna, C. Morath, D. A. Cardimona, and S. W. Kennerly, *Appl. Phys. Lett.* **81**, 1369 (2002).

⁴S. Krishna, G. von Winckel, S. Raghavan, A. Stintz, G. Ariyawansa, S. G. Matsik, and A. G. U. Perera, *Appl. Phys. Lett.* **83**, 2745 (2003).

⁵S. Chakrabarti, X. H. Su, P. Bhattacharya, G. Ariyawansa, and A. G. U. Perera, *IEEE Photonics Technol. Lett.* **17**, 178 (2005).

⁶W. Z. Shen, A. G. U. Perera, H. C. Liu, M. Buchanan, and W. J. Schaff, *Appl. Phys. Lett.* **71**, 2677 (1997).

⁷D. G. Esaev, M. B. M. Rinzan, S. G. Matsik, A. G. U. Perera, H. C. Liu, B. N. Zhonkov, V. I. Gavrilenko, and A. A. Belyanin, *J. Appl. Phys.* **95**, 512 (2003).

⁸S. Adachi, *Phys. Rev. B* **35**, 3454 (1986).

⁹M. D. Sturge, *Phys. Rev.* **127**, 768 (1962).

¹⁰S. K. Zhang, W. B. Wang, I. Shtau, F. Yun, L. He, H. Morkoç, X. Zhou, M. Tamargo, and R. R. Alfano, *Appl. Phys. Lett.* **81**, 4862 (2002).

¹¹F. Binet, J. Y. Duboz, E. Rosencher, F. Scholz, and V. Harle, *Appl. Phys. Lett.* **69**, 1202 (1996).

¹²S. G. Matsik, M. B. M. Rinzan, D. G. Esaev, A. G. U. Perera, H. C. Liu, and M. Buchanan, *Appl. Phys. Lett.* **84**, 3435 (2004).